JGR Space Physics

RESEARCH ARTICLE

10.1029/2020JA028424

Key Points:

- High altitude echoes observed in the topside ionosphere over Jicamarca at postmidnight times during solar minimum
- The echoes inhabit altitudes between 1,000 and 2,200 km
- High altitude echoes exhibit spectral sidebands at the lower-hybrid frequency

Correspondence to:

S. Derghazarian,
sd779@cornell.edu

Citation:

Derghazarian, S., Hysell, D. L., Kuyeng, K., & Milla, M. A. (2021). High altitude echoes from the equatorial topside ionosphere during solar minimum. *Journal of Geophysical Research: Space Physics*, *126*, e2020JA028424. https://doi.org/10.1029/2020JA028424

Received 29 JUN 2020
Accepted 17 DEC 2020

High Altitude Echoes From the Equatorial Topside Ionosphere During Solar Minimum

S. Derghazarian[1], D. L. Hysell[1], K. Kuyeng[2], and M. A. Milla[2]

[1]Earth and Atmospheric Sciences, Cornell University, Ithaca, NY, USA, [2]Jicamarca Radio Observatory, Lima, Peru

Abstract We describe a new class of nonthermal plasma density irregularities observed in the postmidnight topside equatorial ionosphere under low solar flux conditions. They are distinct from irregularities associated with equatorial spread *F* (ESF) in terms of their morphology and because they exhibit strong spectral sidebands at the lower-hybrid frequency. The coherent echoes were observed in a series high-altitude radar experiments performed at Jicamarca utilizing long- and coded double-pulse modes and a dual-beam mode. The coded double-pulse mode was used to measure the low-frequency characteristics of the echoes with fine range resolution. Doppler shifts of the main backscatter line were observed to fall between ±150 m/s. The long-pulse mode was employed for high-frequency spectral analysis which revealed the presence of strong spectral sidelobes at the lower-hybrid frequency. A dual-beam mode was used to investigate the horizontal structure of the echoes. Zonal drift speeds of 50–70 m/s were inferred with this mode, and longitudinal dimensions of approximately 270 km were estimated. The study summarizes with a discussion of different mechanisms that may be responsible for the phenomenon and the lower-hybrid sidebands in particular.

1. Introduction

Plasma density irregularities in the upper atmosphere have been studied extensively using radio and radar techniques since the dawn of the space age. When caused by thermal fluctuations in a plasma in equilibrium, these irregularities form the basis of incoherent scatter radar (ISR) techniques (D. T. Farley et al., 1961). However, when the irregularities are due to nonthermal effects, much stronger (e.g., up to seven orders of magnitude in case of ESF [D. Farley et al., 1970]) coherent scatter may be observed. Sources of coherent scatter at the magnetic equator include electron density irregularities driven by neutral turbulence in the mesosphere (Rastogi & Bowhill, 1976), irregularities driven by gradient drift (Rogister & D'Angelo, 1970; Sudan et al., 1973) and Farley-Buneman instabilities (Buneman, 1963; D. T. Farley 1963) in the equatorial electrojet (Forbes, 1981), and the so-called 150-km echoes (Balsley, 1964; Chau & Kudeki, 2006; Chau et al., 2013; Kudeki & Fawcett, 1993) in the equatorial valley region thought to be related to the upper-hybrid instability (Lehmacher et al., 2020; Longley et al., 2020). In the postsunset equatorial *F* region, equatorial spread *F* (ESF) (Booker & Wells, 1938; Hysell et al., 2000; Woodman., 2009) is a commonplace phenomenon characterized by plasma irregularities with scale sizes ranging from centimeters to several hundreds of kilometers and altitudes that can reach up to about 1,500 km (D. Farley et al., 1970) during quiet periods and higher during geomagnetic storms.

Coherent echoes from even higher altitudes above 1,500 km in the inner plasmasphere were discovered recently by accident when they contaminated noise samples in high-altitude ISR data (Hysell et al., 2019). The echoes took the form of thin layers rather than convective plumes and occurred mainly in the predawn sector. Unlike coherent scatter associated with ESF which occurs at all solar flux levels, these high-altitude echoes have been observed only during low solar-flux conditions. Most significantly, we will show that the high-altitude echoes in question exhibit strong sidebands at the lower-hybrid frequency for protons. They thus constitute a new phenomenon.

In this paper, we present findings from a series of dedicated radar experiments run during the fall and spring of 2018 and 2019 to probe the high-altitude echoes. The spatial, temporal and spectral characteristics of the echoes will be described and evaluated. Subsequently, we discuss some well-known irregularities and instabilities associated with the production of lower hybrid waves and evaluate their relevance for our

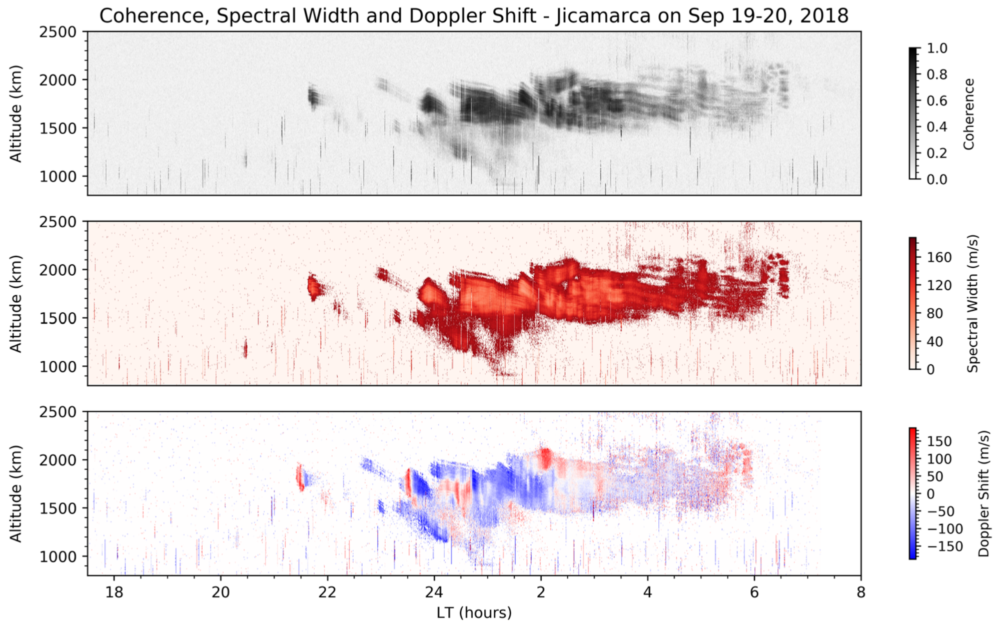

Figure 1. Examples of high-altitude scattering layers. The upper panel indicates coherence, the middle panel spectral width, and the lower panel line-of-sight Doppler shift. Short lived echoes in the bottom half of the panels are due to space debris which has not been removed.

observations. These include Lower Hybrid Solitary Structures (LHSS), VLF mode conversion, and lower hybrid drift instability. Finally, we conclude with a summary of our findings and plans for future experiments.

2. Experimental Methodology and Results

Figure 1 shows observations of the high-altitude scattering layers made on September 19 and 20, 2018. The observations were made with a double-pulse mode. Each pulse in the pair employed a 13-bit Barker code with a baud width of 100 μs. The lag between pulses was 4 ms. This is several times longer than the correlation time for incoherent scatter at 50 MHz. A single circular polarization was used for transmission. Sampling was performed at 50 μs intervals, and the incoherent integration time was 15 s. The double-pulse coherence was calculated from the modulus of the normalized autocorrelation function at the 4-ms lag. Noise removal was not performed in the normalization, and so the coherence is a measure both of the correlation time of the echoes and the signal-to-noise ratio (D. T. Farley, 1969). The coherence gives a visual representation of the distribution of the irregularities in range and time.

The echoes presented first as small patches, intermittently spaced in range and time, followed by a much larger structure that spanned altitudes between 1,000 and 2,200 km, appearing shortly before midnight and persisting significantly until local sunrise at ground level (≈0600 LT). Considerable fine structure was present in the backscatter at times. Horizontal streaks were evident for the last few hours of the event. This could well be an indication of structures drifting slowly through the radar beam and persisting for a long duration rather than layers per se.

The Doppler shifts and spectral widths shown in the second and third panels in Figure 1 were derived from the phase and modulus of the normalized correlation function, respectively, this time including noise subtraction in the normalization such that the results are independent of the signal-to-noise ratio.

Doppler velocities were roughly consistent with range rates and varied from -150 m/s to 150 m/s. The largest Doppler shifts and sharpest variations in range and time occurred around midnight. Variations in the Doppler shift were partially but imperfectly correlated with variations in intensity. Spectral widths were as small as about 40 m/s in the most intense regions of backscatter and increased in the peripheral regions.

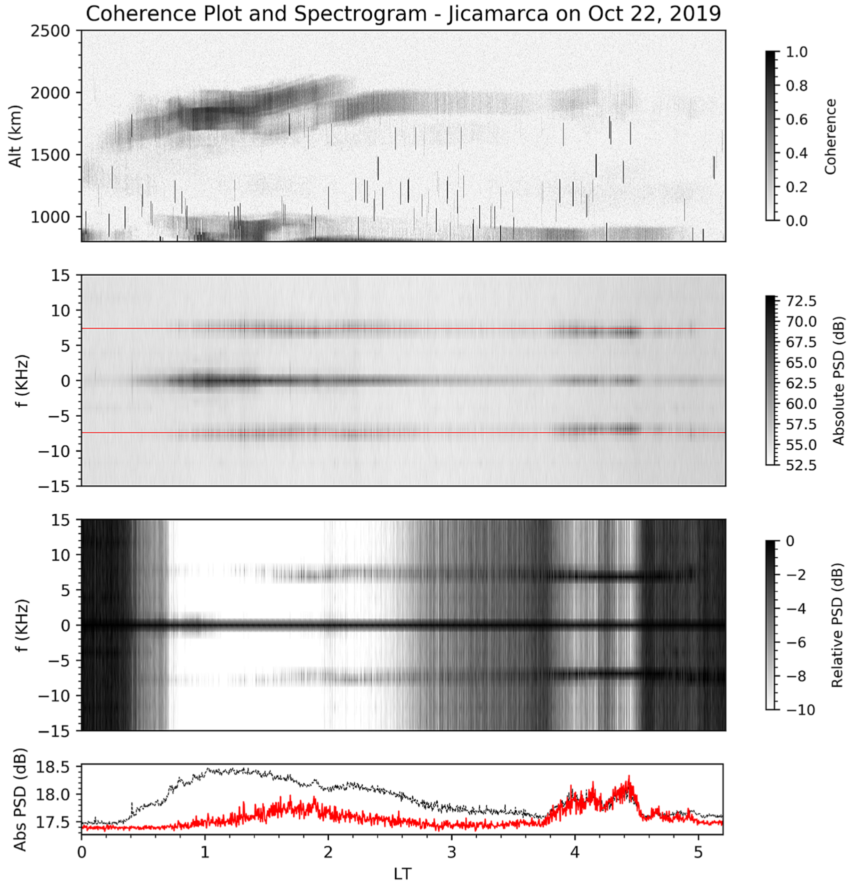

Figure 2. High-altitude echoes received from a 2-ms long pulse experiment conducted on October 22, 2019. Echoes appear predominantly between 0000 and 0300 LT. Altitudes ranged from 1,200 to 2,000 km. The top panel shows the coherence. The middle and lower panels depicts non normalized and normalized spectrograms, respectively, for altitudes near ≈ 1,800 km (see text). The lower panel displays normalized line plots of the zero frequency bin (shown in black) and the 6.8–7.8 KHz bin (shown in red) respectively, indicating the level of correlation between both signals in the spectrogram. The horizontal red lines (7.4 KHz) superimposed on the spectrograms denote the theoretical value of the lower hybrid frequency, calculated from the warm plasma dispersion relation (see Equation 4 in Appendix), at an altitude of 1800 km for typical densities and temperatures present around midnight. The densities and temperatures used were modeled by SAMI2-PE (Varney et al., 2012).

Figure 2 shows several hours of postmidnight observations made on October 22, 2019. For this experiment, a single long pulse with a 2-ms pulse width and a 40-ms IPP was used. Samples were acquired at 1 μs intervals. For analysis comparable to that applied to the September data, we applied a filter with a 100 μs boxcar impulse response function prior to detection. The coherence was calculated using an 800 μs lag time. The range resolution of the experiment was relatively poor compared to the previous one.

The October echoes can be observed to extend from midnight to approximately local sunrise time (0540 LT). Several prominent scattering layers can be seen centered at ≈ 1700, 1800, and 1900 km in Figure 2, and at 1400 and 1500 km in Figure 3. Echoes from ESF were visible at lower altitudes, but they were not obviously related to the high-altitude structures even though they overlapped in time. The poor range resolution of the experiment prevents the detection of fine structure in the layers.

The long-pulse mode permits the calculation of broadband Doppler spectra. We have found only interference at frequencies outside the band between ±15 kHz and so concentrate here on frequencies within this band. The two lower panels in Figure 2 show spectrograms constructed from samples corresponding to the upper scattering layer at 1800-km range. The incoherent integration time used here was 15 s. The center panel shows absolute power spectral density on an arbitrary scale, and the bottom panel shows the relative power spectral density normalized to the power in the zero-frequency bin.

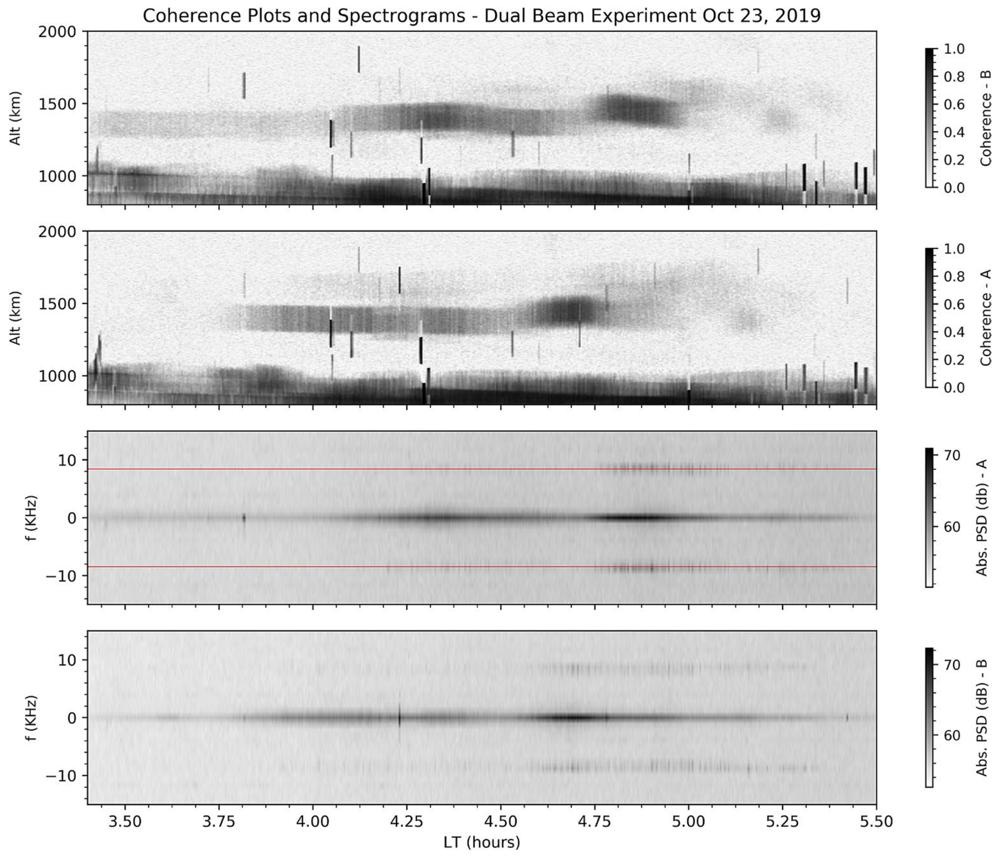

Figure 3. Coherence of echoes from dual-beam experiments conducted on October 23, 2019. Transmitters A (westward) and B (eastward) point to different scattering volumes separated zonally by ≈ 1.5°. The lower two panels depict non normalized spectrograms for altitudes near ≈ 1,400 km (see text). The horizontal red lines (8.4 KHz) superimposed on the spectrogram in the third panel denote the theoretical value of the lower hybrid frequency, calculated from the warm plasma dispersion relation (see Equation 4 in Appendix), at an altitude of 1400 km and for typical densities and temperatures present around 4.5 LT. The densities and temperatures used were modeled by SAMI2-PE (Varney et al., 2012).

The most important features in Figure 2 are the prominent sidebands at Doppler shifts equal to the lower hybrid frequency for protons, about 6–9 kHz depending on the altitude and ambient density, for the entire duration of the echoes. In the center panel, the 6.8–7.8 KHz bin, corresponding to the range of lower hybrid frequencies at ≈1,800 km is most prominent. Higher frequency (7.8–8.8 KHz) and lower frequency (5.8–6.8 KHz) bins are also present. The highest frequency bin decreases in intensity from midnight to 4LT, while the middle and lowest frequency bin increase in intensity as would be expected by the drop in ambient densities from postmidnight to early morning hours. The same result was obtained when samples were taken from the lower scattering layer centered at 1,400 km in Figure 3, with the spectrogram in that case showing slightly higher frequency sidebands consistent with the larger magnetic flux density at lower altitudes (see, e.g., lower two panels of Figure 3).

It is noteworthy also that the ratio of the power in the sidebands to the power in the zero-frequency bin is not constant. For example, the enhancement in the sidebands between about 0350–0430 LT occurred at a time when the overall scattering intensity was diminishing and the layer was dissipating.

Furthermore, an exploded view of a portion of the bottom panel in Figure 2, shown in Figure 4, reveals yet another interesting characteristic of the emissions—that of significant, persistent fluctuations in amplitude. A comparison of these fluctuations in the lower hybrid sidebands to those in the zero frequency bins (not shown here) shows that they are synchronized, demonstrating the fact that the fluctuations are not a form of enhanced hybrid lines in the incoherent scatter spectrum.

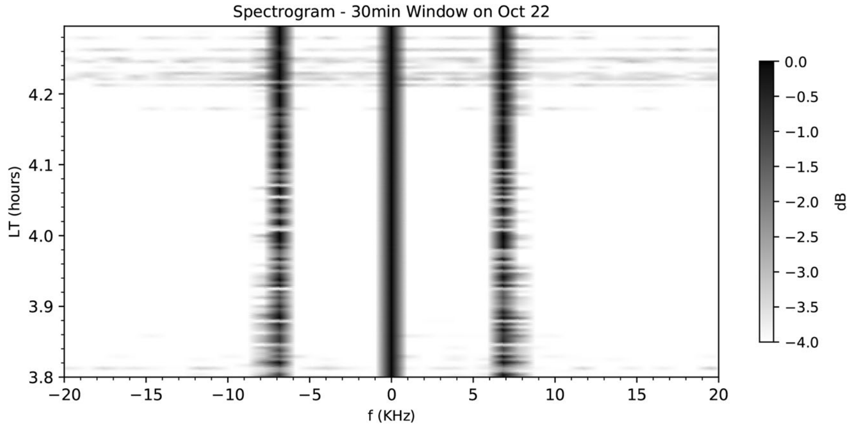

Figure 4. Exploded spectrogram for times between 0348 and 0412 LT and ≈1800 km. Dramatic intensity variations of the lower hybrid waves in time can be seen.

The characteristic frequency derived from the homogeneous lower hybrid dispersion relation (as shown in Appendix A) was superimposed onto the spectrogram in Figure 2 using a thin red line. To arrive at this frequency, we used magnetic field intensity values from IGRF-13, assumed a nighttime electron density value consistent with measurements shown in Hysell, Milla, et al. (2017), and selected a nominal temperature of 1000 K. Employing the homogeneous approximation to calculate the characteristic frequency is justifiable to the extent the influence of plasma inhomogeneities on wave propagation and instability is small (Treumann & Baumjohann, 1997).

Dual-beam experiments were conducted on October 23 and 24, 2019, to infer the zonal drifts and zonal extent of the high-altitude scattering regions. The two beams used orthogonal linear polarizations. Beams A and B were pointed westward and eastward, respectively, with a separation of about 1.5° or by a little more than two individual beamwidths. The magnetic declination of the pointing positions was about the same for each beam (see Figure 5).

On October 23, 2019, the echoes ranged from just 1,200 to 1,500 km altitude. To estimate drifts, we measured the shift in time of apparently common features in the two upper panels of Figure 3. The region with the highest coherence appeared in the westward-pointing beam approximately 15 min before appearing in the eastward-pointing beam. This was also the region with the strongest lower-hybrid lines. The zonal distance

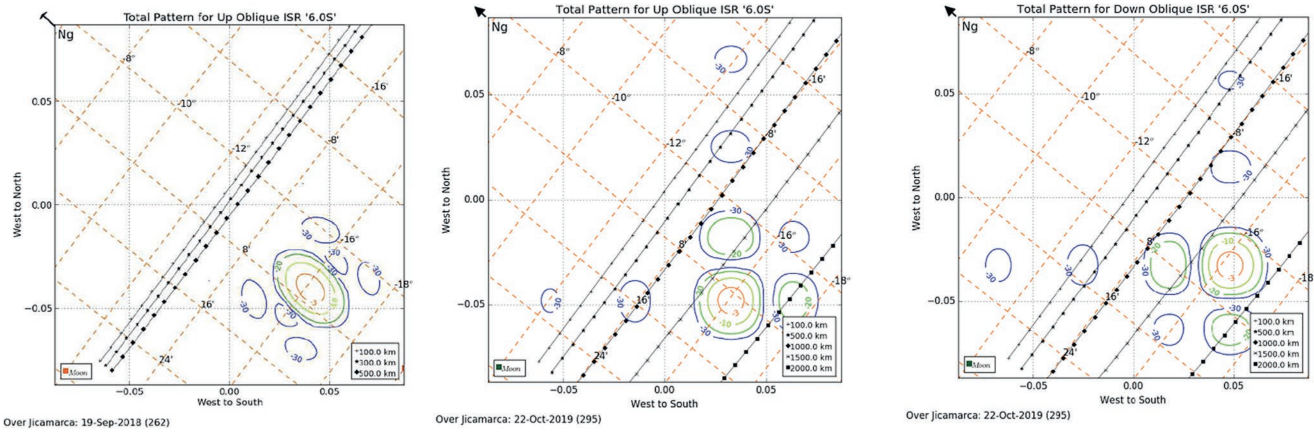

Figure 5. The leftmost panel shows the transmitter main lobe and sidelobe positions for the Barker coded double pulse experiment on September 19–20, 2018. The center and right panels show the main lobe and sidelobe positions for the westward and eastward transmitters respectively, used in the dual beam experiments on October 23 and 24, 2019. An angle of ≈1.5° separates them. The configuration for the long pulse experiment with a single pointing position is not shown in this figure but is similar to the leftmost panel.

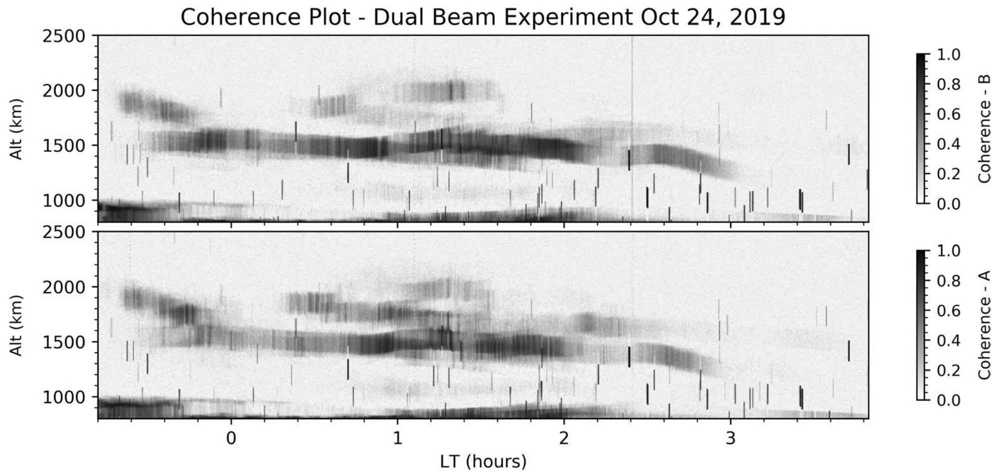

Figure 6. Echoes from dual-beam experiments conducted on October 23 and 24, 2019.

between the positions where the layer intersected the two antenna beams was about 35 km–40 km. These figures imply a zonal drift speed of about 45–50 m/s eastward.

On October 24, 2019, as shown in Figure 6, the echoes were more spread in altitude. Between 0100 and 0130 LT, three different height ranges were occupied by scatterers: 1,200–1,500 km, 1,500–1,700 km, and 1,750–2,000 km. In contrast to the previous day, many of the features appear nearly identical in both beams, while others appear to be drifting eastward at about 70 m/s. The data are fairly ambiguous, however, and the apparent motion of the scatterers only approximates the true motion to the extent that the scatterers evolve slowly. On both October 23 and 24, 2019, the coherence measured with beams A and B exhibited similar if shifted features. This suggests that the underlying structure evolved with relatively long timescales.

The longitudinal dimensions of the scattering structures can be estimated by multiplying the average drift speed by the duration of the echoes observed in either one of the beams. To simplify the analysis, we consider only the experiment on October 23, 2019, when the totality of the structure appeared to be drifting eastward at a uniform speed. In this case, the longitudinal extent can be estimated to be about 270 km.

3. Overview of Ionospheric Processes Associated with Lower Hybrid Waves

The discovery of lower hybrid waves in the topside postmidnight equatorial ionosphere/inner plasmasphere prompts a review of other regions and contexts in geospace where lower hybrid waves play significant roles. Several relevant observations and lines of inquiry are described below.

3.1. Lower Hybrid Solitary Structures

LHSS's are axisymmetric and spatially localized structures elongated along magnetic field lines and having perpendicular dimensions that vary from a few to several thermal ion gyroradii (10–100 m at auroral latitudes) (P. Schuck et al., 2003). They are characterized by large amplitude bursts of lower hybrid electrostatic waves having frequencies slightly above and below the lower hybrid resonance (P. Schuck et al., 1998). They reside within density depletions that vary from a few percent to several tens of percent of the background electron density (Knudsen et al., 1998; McAdams et al., 1998) and found to exhibit a Gaussian density profile (Hoymork et al., 2000). They are frequently observed at auroral latitudes. The first definite observations of LHSS's were made by the MARIE sounding rocket (Lebelle et al., 1986). It was found that the peak electric field associated with the structures was several times larger than the background VLF hiss. In auroral regions, LHSS's were observed by the Freja satellite at altitudes ranging from 1,450 to 1,750 km (Dovner et al. 1994; Eriksson et al., 1994). Both satellite and sounding rocket data have revealed that LHSS's always appear whenever VLF hiss is present (Dovner et al., 1997; Lynch et al., 1999).

Currently, two classes of theories are applied to LHSS's: linear and nonlinear. The nonlinear treatments center on modulational instability, lower hybrid collapse, and strong turbulence. The first treatment is based on the parametric instability of a lower hybrid pump wave to low frequency density fluctuations in a homogeneous plasma in which the density fluctuations are assumed to be triggered by a modulational instability (Chang, 1993; V. Shapiro et al., 1993). The pump wave follows a homogeneous lower hybrid dispersion relation, and the instability of the wave results in its decay into other lower hybrid waves and lower frequency density fluctuations (Shukla et al., 1994). However, a study by Pécseli et al. (1996) eliminates the possibility of this instability being the driving mechanism in LHSS's by demonstrating that LHSS's are not spaced at regular intervals as predicted by the modulational instability but follow a Poisson distribution. The second treatment, lower hybrid collapse, rests on the assumption that the density depletions and lower hybrid waves are both related to a parallel electron ponderomotive force produced by a high frequency electron $E \times B$ drift (Musher & Sturman, 1975a, 1975b; V. Shapiro et al., 1993). Statistical studies comparing the collapse theory with Freja satellite data, however, have shown that this theory is also incompatible with experimental data (Pécseli et al., 1996). Robinson (1999) attempted to rectify these discrepancies of the collapse theory by resorting to the theory of strong turbulence which assumes a four phase nucleation cycle that includes nucleation, collapse, arrest and relaxation (Doolen et al., 1985; Robinson et al., 1996, 1999). However, a statistical study of LHSS's in the auroral ionosphere performed by P. W. Schuck et al. (2002) does not support this theory.

The linear class of theories explain the production of lower hybrid waves in LHSS's by mode conversion of VLF auroral hiss to lower hybrid eigenmodes of preexisting density depletions through linear scattering off of density irregularities (Pinçon et al., 1997; P. W. Schuck & Seyler, , ; P. Schuck et al., 1998). Previous studies (Bell & Ngo, 1988; Inan & Bell, 1985; Titova et al., 1984) presented satellite data showing that lower hybrid waves are commonly stimulated by VLF whistlers interacting with field aligned density irregularities with wavelengths of the order of the lower hybrid waves. The dispersive properties of the eigenmodes are then modified by the inclusion of the Hall current generated by the $E \times B$ drift which accounts for most of the spectral characteristics of LHSS's observed experimentally (P. Schuck et al., 2003). No diamagnetic currents or drift waves are needed despite the assumption of plasma inhomogeneity (P. Schuck et al., 1998). Studies by Seyler et al. (1994) and P. Schuck et al. (1998) explain LHSS's with linear theory applied to an inhomogeneous cold plasma composed of preexisting cylindrical density depletions. The cylindrical nature of the density depletions motivates the choice of cylindrical basis functions, decomposing the lower hybrid waves into right and left hand rotating modes relative to the magnetic field. A consequence of this theory is wave solutions that consist of a continuous spectrum of waves above the lower hybrid resonance (LHR) outside the density depletions of the LHSS's and a discrete spectrum of waves below the LHR inside the density depletions. The predictions of linear theory generally agree with interferometric (Bonnell et al., 1998) and spectral analyses (Kjus et al., 1998; Pécseli et al., 1996; 1997) of the electric fields within the structures.

In addition to the assumptions of linear theory, there is every reason to believe that azimuthal ion currents within density depletions also participate in the excitation of lower hybrid waves. Ions are presumed to play a role in the instabilities because of numerous observations by sounding rockets (Lynch et al., 1996; Vago et al., 1992) in which Transversely Accelerated Ions (TAI) were found with higher energies inside LHSS's as compared to the general background values. Data from TOPAZ-III has in fact revealed direct correlations between TAI's, enhanced electric field fluctuations and density depletions in thousands of LHSS's (Arnoldy et al., 1992). The contribution of the ion current to the excitation of lower hybrid waves in LHSS's was investigated by Vakim et al. (1997). The study found that an azimuthal ion current in a density cavity could lead to a positive growth rate through the Cherenkov interaction of resonant ions with the waves. The cavity considered was radially inhomogeneous and followed a Gaussian density profile. Chibisov and Mikhailenko (2012) and Aarenkov et al. (2019) investigated the special case of a radially inhomogeneous ion ring distribution within a homogeneous plasma. They also found that when certain conditions were met, an instability was triggered, leading to the growth of lower hybrid waves.

In studies by Malingre et al. (2008) and Berthelier et al. (2008), LHSS's were found for the first time at equatorial latitudes. They were discovered following the detection of lower hybrid waves by the DEMETER satellite at equatorial latitudes in large scale, deep density depletions spanning several hundreds of kilometer longitudinally and with densities two to three orders of magnitude lower than that of the surrounding plasma. These emissions were associated with bursts of thermal ions, narrowband electromagnetic ELF waves and shown to evolve into large amplitude quasimonochromatic wave packets that bore resemblance to those observed in LHSS's at auroral latitudes. The scale length of the irregularities contained within depletions were found to be 10 m across and 40 m along the field lines when $\Delta n_i/n_i \approx 10\%$. Berthelier et al. (2008) found the phenomena in the nighttime ionosphere between 2000 and 2300 LT and both studies indicated that the density depletions were associated with periods of disturbance in the geomagnetic field. The experimental data suggested that the interaction of the depletions with whistlers generated through tropospheric lightning discharges below the orbital path of the satellite was the source of the lower hybrid emissions.

The similarities observed between auroral and equatorial LHSS's suggest they both share the same underlying physics. In both cases they are observed in regions of strong VLF noise and in underdense plasmas ($\omega_{\mathrm{pe}} < \omega_{\mathrm{ce}}$). However, the energy source of the background hiss present at equatorial latitudes is very different from that responsible for auroral hiss, with the former presumed to be caused by energetic electrons (Kintner, 1992) and the latter by lightning generated whistlers. A unique feature of the equatorial LHSS's is the presence of narrowband ELF.

Similarly to the earlier studies in auroral regions and mid-latitudes, Berthelier et al. (2008) highlighted two possible mechanisms for the excitation of lower hybrid waves in equatorial density depletions. The first is a linear process involving mode conversion of electromagnetic whistlers scattering off of preexisting density depletions. The second mechanism is through a parametric instability in which the density depletions and lower hybrid waves are generated concurrently (Lee et al., 1984). The electric field measurements in Malingre et al.(2008) however, do not support the nonlinear explanation.

3.2. Lower Hybrid Drift Instability

Another possible mechanism for the generation of the echoes is a lower hybrid drift instability. Temperature and/or density gradients in an inhomogeneous plasma give rise to a diamagnetic drift which couples with a drift wave leading to an instability through inverse Landau damping (Huba et al., 1981). To arrive at an expression for the growth rate of the instability, perturbed quantities were assumed to vary linearly, the analysis was restricted to electrostatic phenomena where $\beta \ll 1$ ($\beta = 8\ nT/B^2$), and only oscillations perpendicular to B were considered. A fundamental requirement for the instability is that electrons be magnetized and ions unmagnetized. Thus, a simple expression for the ion demagnetization condition in a collisional plasma was given by $\frac{\nu_{ii}}{\Omega_i} k^2 r_{Li}^2 \leq 1$ where r_{Li} denotes the ion gyroradius and ν_{ii} the ion-ion collision frequency (Huba & Ossakow, 1979). Ion-ion collisions, which appear in the ν_{ii} term above, contribute to the demagnetization process by pushing the ions across magnetic field lines, a crucial step in exciting the instability through resonance with the perpendicular drift wave. They also set a critical background density value. On the contrary, all other collisions (electron-ion, electron-electron and electron-neutral), lead to a damping of the wave, setting an upper threshold to the density scale length (L_n) given by $L_n < r_{Li}\sqrt{(k v_{thi} / \nu_e)}$. The ion demagnetization condition and scale length threshold are the two important parameters which determine the viability of the lower hybrid drift instability for specific irregularity wavelengths and altitudes. For the 0.36 m and 0.11 m irregularities seen by the ALTAIR and Tradex radars on Kwajalein Atoll, the minimum densities required are 2×10^9 m−3 and $2 \times 10^8\ \mathrm{m}^{-3}$ respectively. Thus, the lower hybrid drift instability is operable at ranges where high altitude echoes at Jicamarca are observed. However, for the 3 m irregularities seen by Jicamarca, the minimum density required is $> 10^{11}\ \mathrm{m}^{-3}$, in addition to extremely sharp scale lengths of less than 15 m. Both of these conditions are not satisfied at the topside or lower plasmaspheric altitudes above Jicamarca and lead us to consider the possibility of other mechanisms, possibly remote coupling, working in conjunction with the lower hybrid drift instability.

4. Discussion

The data presented in this preliminary study is insufficient to support a conclusion regarding which of the processes reviewed in the previous section is responsible for the high altitude irregularities observed over Jicamarca.

For example, to determine whether the structures can be categorized as LHSS's, more detailed information about the longitudinal and field-aligned dimensions of the structures would be needed. This could be gathered, for example, using a fully steerable radar like ALTAIR that could provide longitudinal mapping of the structures. Finer spatial resolution is also necessary to accurately measure the transverse dimensions and determine whether the larger structures are a discontinuous collection of smaller ones with dimensions characteristic of LHSS's. If further radar experiments prove that the high-altitude echo phenomenon is ubiquitous, sun synchronous satellite data at the appropriate altitudes could be useful for a statistical study of the dimensions of the echoes along field lines and its electric field fluctuations.

Whether simple VLF mode conversion is taking place without all of the other associated characteristics of equatorial LHSS's is another hypothesis worth exploring. This assumption cannot be discounted because not all studies provide conclusive evidence that observed lower hybrid wave emissions from field aligned irregularities are indicative of LHSS's. To verify this hypothesis we cannot use radar data alone since VLF hiss is predominantly electromagnetic whereas the radar can only observe electrostatic phenomena. Simultaneous radar and sounding rocket experiments would be needed in order to determine if a correlation exists between lower hybrid wave power and the presence of background hiss. A spectral analysis of the hiss would further indicate whether it is lightning-induced or the result of equatorial hiss (Morgan, 1979).

The direct involvement of a lower hybrid drift instability in the generation of 3-m irregularities at Jicamarca was mainly discounted in the previous section. However, measurements from higher frequency equatorial radars such as ALTAIR and Tradex could shed light on whether a cross-scale coupling mechanism between the irregularities exists.

It is also interesting to note that gyrolines naturally present in the ISR spectra tend toward the lower hybrid resonance when the aspect angle approaches zero. In a study by Hysell et al. (2017), gyrolines were shown to appear in ISR spectra processed from Arecibo data in the 100–200 km range interval. Whether these lines are also present in the ISR spectra above Jicamarca, for aspect angles close to zero and for ranges where the high altitude echoes are observed, would need to be examined. If this is the case, it would suggest the possibility that the lower hybrid sidebands are an enhancement of the lower hybrid line feature naturally present in the ISR spectra, by means of an instability.

5. Summary and Conclusions

We have presented data from experiments conducted to probe a new class of nonthermal 3-m plasma density irregularities causing VHF radar echoes in the equatorial topside/inner plasmasphere, mainly in the postmidnight sector. The echoes were characterized in terms of their gross morphology and low-frequency spectral moments. Their characteristics were broadly similar to those of irregularities generated in the topside by convective instability related to ESF. However, the echoes were also found to exhibit strong sidebands at the lower hybrid frequency, something which has not been observed before. It is unclear at this point whether the sidebands are an incidental feature of density irregularities which happen to form in the topside or a crucial component of the process responsible for creating the irregularities in the first place.

Various well-known phenomena involving lower-hybrid waves in the ionosphere were reviewed as possible candidates to help explain the irregularities. The most important features of the irregularities observed are the following:

1. Irregularities appear in the predawn sector of the topside ionosphere and lower plasmasphere and form structures that most often span altitudes in the range of 1,500–2,200 km
2. Coherence varies throughout the structures, and the irregularities dissipate entirely before local sunrise
3. Lower hybrid waves are present for the entire duration and range of altitudes where the high altitude irregularities are observed, and were not detected within the ESF present at lower altitudes. A very large increase in relative intensity was noted in portions of the echoes between 0400 and 0500LT on October 22, 2019, where the lower hybrid sideband intensity became comparable to that of the zero frequency bin, even as the structures had almost dissipated
4. Only eastward zonal drifts were observed from 50 –70 m/s
5. Zonal dimensions of several hundred km were calculated

6. Line of sight Doppler shifts vary from −150 m/s and 150 m/s and have been observed to change orientation frequently within the structures present in the September 20, 2018 postmidnight sector. More experiments are needed to determine whether this phenomenon is commonplace. The Doppler shifts tracked the range rates of the echoes
7. Structures appear to be distinct from ESF but occur at similar postmidnight times. The echoes only appear in patches shortly before midnight in contrast to ESF

Additional experiments involving radar interferometry and imaging, long pulse codes for overspread targets, bistatic measurements for inferring meridional drifts, aspect sensitive experiments, and supporting in situ measurements are required for investigating the irregularities further.

Radar interferometry and imaging (Hysell & Chau, 2006) can be used to visualize fine structures within the scattering volume in three dimensions. The long and double pulse experiments suffered from tremendous ambiguity with respect to the spatial distribution of structures. Imagery in the meridional direction would yield an estimate of the magnetic aspect sensitivity of the lower-hybrid lines.

Using long coded pulses, for example, alternating codes, the lower-hybrid spectra could be resolved finely in range. This would allow us to investigate the transverse structure and dimensions of the lower-hybrid waves more finely. In addition, it would give us the ability to measure changes in the lower hybrid frequency due to the ambient density drop from midnight to early morning local times. This could potentially be a novel method for measuring densities at high altitudes in the postmidnight sector.

Radar measurements of bulk drifts and dimensions along field lines would give additional information on the structures. In order to make this experiment possible, we would need to use a bistatic or multistatic system such that the condition for field-aligned scatter could be met at multiple points along a field line.

Additional experiments could be carried out using ALTAIR and Tradex to gain information about the irregularities at shorter wavelengths. This would prove important for isolating the processes responsible for their generation. In addition, the echoes could be mapped continuously in space using the steerability of these systems.

Our understanding of the structures can also be considerably improved by comparing radar data with that gained by satellites and sounding rockets. One of the limitations of radar experiments is the need to compromise between spectral resolution and range resolution. Both instruments can be used to gather more detailed spectral and electron density measurements. Sounding rockets especially can be launched simultaneously during radar experiments and provide direct comparisons with radar data. Satellite conjunctions are difficult to manage as a rule, but if the irregularities prove to be as ubiquitous as they now seem, finding them could be practical.

Further investigation is needed to determine whether ESF conditions favor the emergence of the high-altitude irregularities. Additional observations should be made during June equinox when ESF conditions are relatively unlikely to occur in the Peruvian sector.

Finally, numerical simulations of cross-scale coupling between irregularities of different wavelengths, and numerical verification of the existence and possibility of enhancement of lower hybrid lines for the altitudes at which the irregularities in this study were observed, will be explored in more detail in a subsequent manuscript.

Appendix A: Dispersion Relation of Lower Hybrid Waves in Homogeneous Plasma

In this section we derive an approximate dispersion relation for lower hybrid electrostatic waves in a homogeneous plasma. We follow a similar procedure to the one used in (Hysell, Vierinen, et al., 2017). Since the dominant ion is H^+ at the altitudes at which the echoes were observed, that is from 1,200 km to 2,200 km, we simplify the analysis considerably by assuming a two species plasma (electrons and H^+). The expression for the cold plasma lower hybrid resonance frequency given by Swanson (2003) is:

$$\omega_{LH}^2 = \omega_{ce}\omega_{ci}\left(\frac{\omega_{pe}^2 + \omega_{ce}\omega_{ci}}{\omega_{ce}^2 + \omega_{pe}^2}\right) \tag{1}$$

which includes a dependence on the magnetic field, electron density and ion species but excludes kinetic effects. Since $\Omega_i^2 \ll \omega^2 \ll \Omega_e^2$ at LH frequencies, we can treat the ions as unmagnetized and the electrons as magnetized.

The longitudinal projection of the dielectric tensor (dielectric response function) is given by:

$$K = 1 + \frac{1}{k^2\lambda_{de}^2}\left[1 + \sum_{n=-\infty}^{\infty} \frac{\omega}{\sqrt{2}k_{\|}v_{te}} \Lambda_n(\eta^2) Z(\Theta')\right] + \frac{1}{k^2\lambda_{di}^2}[1 + \theta Z(\theta)] \tag{2}$$

where N is the number of ion species, $\theta = \frac{\omega / k}{\sqrt{2}v_{th}}$ and $\Theta' = \frac{\omega - n\Omega_e}{\sqrt{2}k_{\|}v_{te}}$ are the normalized ion and electron velocities respectively, $v_{te} = \sqrt{K_BT / m_e}$ is the thermal electron velocity, $\eta^2 = \frac{k_\perp^2 v_{te}^2}{\Omega_e^2}$, $cos^2\beta = \frac{k_{\|}^2}{k^2}$ with β representing the angle between the k vector and B, and Z is the plasma dispersion function. Note that the second term in the dielectric response function is the electron susceptibility, and the last term is the ion susceptibility.

Using the large Θ' approximation for $Z(\Theta')$ (since $k_{\|}v_{th} \ll \omega$): $Z(\Theta') \approx i\sqrt{\pi}e^{-\Theta'^2} - \Theta'^{-1}(1 + \frac{1}{2\Theta'^2} + \ldots)$, in conjunction with the expansion form of the modified Bessel function $I_n(\eta^2)$ for small η^2 (since $k_\perp v_{th} \ll \Omega_e$): $I_n(\eta^2) = (\frac{1}{2}\eta^2)^n \sum_{k=0}^{\infty} \frac{(\frac{1}{4}\eta^4)^k}{k!(n+k)!}$, we can rewrite a more simple approximation for the electron susceptibility. Since the n = 0 term is dominant in Equation 2, to first approximation, the real part of the electron susceptibility can be written as:

$$\begin{aligned} Re(\chi_e) &= \frac{1}{k^2\lambda_d^2}\left[1 - \left(1 - \eta^2 + \frac{3}{4}\eta^4 + \ldots\right)\left(1 + \frac{k_{\|}^2 v_{te}^2}{\omega^2} + 3\frac{k_{\|}^4 v_{te}^4}{\omega^4} + \cdots\right)\right] \\ &\approx \frac{\omega_{pe}^2}{\omega^2}\left[\frac{\omega^2}{\Omega_e^2} - cos^2\beta\left(1 + 3\frac{k_{\|}^2 v_{te}^2}{\omega_{LH}^2}\right) + \cdots\right] \end{aligned}$$

where the ω^4 term was replaced by $\omega^2\omega_{LH}^2$ with the help of Equation 1. Following the same procedure for the ion susceptibility and using the large angle approximation for $Z(\theta)$:

$$\begin{aligned} Re(\chi_i) &\approx \frac{\omega_{pi}^2}{k^2 v_{ti}^2}\left[-\frac{k^2 v_{ti}^2}{\omega^2} - \frac{3k^4 v_{ti}^4}{\omega^2\omega_{LH}^2} + \cdots\right] \\ &\approx \frac{\omega_{pi}^2}{\omega^2}\left[-1 - \frac{3k^2 v_{ti}^2}{\omega_{LH}^2} + \cdots\right] \end{aligned}$$

Note that the parameters $\frac{k_\perp^2 v_{te}^2}{\Omega_e^2}$, $\frac{k_{\|}^2 v_{te}^2}{\omega^2}$, and $\left|\frac{k_{\|}}{k_\perp}\right|$ were only retained up to second order. After combining the electron and ion susceptibilities into Equation 2, the dielectric response function becomes:

$$K \approx 1 + \frac{\omega_{pe}^2}{\omega^2}\left[\frac{\omega^2}{\Omega_e^2} - cos^2\beta\left(1 + 3\frac{k_{\|}^2 v_{te}^2}{\omega_{LH}^2}\right)\right] + \frac{\omega_{pi}^2}{\omega^2}\left[-1 - \frac{3k^2 v_{ti}^2}{\omega_{LH}^2}\right] + \cdots \tag{3}$$

The wave frequency can be derived by setting $K = 0$:

$$\omega_r^2 \approx \left[\omega_{pi}^2\left(1+\frac{3k^2v_{ti}^2}{\Omega_e^2\Omega_i^2}\right)+\omega_{pe}^2cos^2\beta\left(1+3\frac{k_\parallel^2v_{te}^2}{\Omega_e^2\Omega_i^2}\right)\right]/\left(1+\frac{\omega_{pe}^2}{\Omega_e^2}\right) \tag{4}$$

where we ignore the imaginary part since $\omega_r \gg \gamma$.

Growth Rate of Lower Hybrid Waves in a Homogeneous Plasma

To estimate the growth rate of the lower hybrid waves in a homogeneous plasma, we include the complex frequency $\omega = \omega_r + i\gamma$ in the expression derived previously for the dielectric tensor and solve for γ, by setting $Im(K) = 0$ and assuming that $\gamma \ll \omega_r$.

We first note that $\Theta_e' \gg 1$, allowing us to drop the term $i\sqrt{\pi}e^{-\Theta_e'^2}$ from the electron plasma dispersion function $Z(\Theta_e')$. In the case of ions, at the altitudes, times and frequencies considered, $\theta_i \approx 7$–8, indicating that the exponential term must be retained. In addition, $\frac{k_\perp^2v_{te}^2}{\Omega_e^2} \ll 1$, justifies the use of $\Lambda_0(\eta^2) \approx 1$. Starting with Equation 2, for a single ion species:

$$\begin{aligned}
Im(K) &= \frac{1}{k^2\lambda_{de}^2}\Lambda_0(\eta^2)Im[(\Theta_e')Z(\Theta_e')] + \frac{1}{k^2\lambda_{d\alpha}^2}Im[(\theta_\alpha)Z(\theta_\alpha)]\\
&\approx \frac{\omega_{pe}^2}{k^2v_{te}^2}\left[\left(1-\frac{k_\perp^2v_{te}^2}{\Omega_e^2}+\cdots\right)\left(\sqrt{\pi}\,Im(\Theta_e'e^{-\Theta_e'^2})+\frac{\Theta_{ei}'}{\Theta_{er}'^3}+3\frac{\Theta_{ei}'}{\Theta_{er}'^5}+\cdots\right)\right]\\
&\quad+\frac{\omega_{p\alpha}^2}{k^2v_{t\alpha}^2}\left(\sqrt{\pi}\,Im(\theta_\alpha e^{-\theta_\alpha^2})+\frac{\theta_{\alpha i}}{\theta_{\alpha r}^3}+3\frac{\theta_{\alpha i}}{\theta_{\alpha r}^5}+\cdots\right)\\
&\approx \frac{\omega_{pe}^2}{k^2v_{te}^2}\left[\left(\frac{\Theta_{ei}'}{\Theta_{er}'^3}+3\frac{\Theta_{ei}'}{\Theta_{er}'^5}+\cdots\right)\right]+\frac{\omega_{p\alpha}^2}{k^2v_{t\alpha}^2}\left(\sqrt{\pi}\,Im(\theta_\alpha e^{-\theta_\alpha^2})+\frac{\theta_{\alpha i}}{\theta_{\alpha r}^3}+3\frac{\theta_{\alpha i}}{\theta_{\alpha r}^5}+\cdots\right)
\end{aligned}$$

Setting $Im(K) = 0$, dividing by $\frac{\omega_{p\alpha}^2}{k^2v_{t\alpha}^2}$, taking into account $\gamma \ll \omega_r$ and $\Theta_e' \gg 1$, the equation can be recast as:

$$\begin{aligned}
0 &\approx \frac{T_i}{T_e}\left(\frac{\Theta_{ei}'}{\Theta_{er}'^3}\right)+\left(\sqrt{\pi}\theta_{\alpha r}Re(e^{-\theta_\alpha^2})+\frac{\theta_{\alpha i}}{\theta_{\alpha r}^3}+3\frac{\theta_{\alpha i}}{\theta_{\alpha r}^5}+\cdots\right)\\
&\approx -\sqrt{\pi}Re\left(e^{-\theta_{\alpha r}^2-2i\theta_{\alpha r}\theta_{\alpha i}}\right)+\frac{\gamma}{\omega_r^3}2k^2\left[\frac{T_i}{T_e}cos^2(\beta)v_{te}^2-v_{t\alpha}^2\left(1+\frac{3}{\omega_r^2}\right)\right]\\
&\approx -\sqrt{\pi}\omega_r^3(e^{-\theta_{\alpha r}^2})cos(-2\theta_{\alpha r}\theta_{\alpha i})+\gamma 2k^2\left[\frac{T_i}{T_e}(cos^2(\beta)v_{te}^2)-v_{t\alpha}^2\right]
\end{aligned}$$

where we replaced the normalized velocities by $\Theta_{ei}' = \frac{\gamma}{kcos(\beta)\sqrt{2}v_{te}}$ and $\theta_{\alpha i}' = \frac{\gamma}{k\sqrt{2}v_{t\alpha}}$ except for the exponential terms, and ignored the term $\frac{3}{\omega_r^2}$ since it is $\ll 1$. Since γ cannot be factored from the cosine term above, we will leave it on the right side of the equation to obtain:

$$\gamma \approx \frac{\omega_r^3\sqrt{\pi}(e^{-\theta_{\alpha r}^2})cos(-2\theta_{\alpha r}\theta_{\alpha i})}{\left(\frac{T_i}{T_e}(2k^2cos^2(\beta)v_{te}^2)-2k^2v_{t\alpha}^2\right)}$$

When we consider $\beta \approx 90^o$, and values of $\frac{\theta_{\alpha i}}{\theta_{\alpha r}} \ll 0.1\%$, which was verified numerically for k < 6, $cos(-2\theta_{\alpha r}\theta_{\alpha i}) \approx 1$ and the expression simplifies to:

$$\gamma \approx \frac{-\left(\omega_r - \boldsymbol{k}\cdot\boldsymbol{u_i}\right)^3 \sqrt{\pi}\,(e^{-\theta^2_{\alpha r}})}{2k^2 v^2_{t\alpha}} \tag{5}$$

where a drift $\boldsymbol{u_i}$ was included.

Data Availability Statement

Data used for this publication are available through the Madrigal database (see http://www.openmadrigal.org.), and found under Jicamarca ISR experiments.

Acknowledgments
The Jicamarca Radio Observatory is a facility of the Instituto Geofisíco del Perú operated with support from NSF award AGS-1732209 through Cornell. The help of the staff is much appreciated.

References

Arnoldy, R., Lynch, K., Kintner, P. M., Vago, J., Chesney, S., Moore, T. E., & Pollock, C. J. (1992). Bursts of transverse ion acceleration at rocket altitudes. *Geophysical Research Letters*, *19*(4), 413–416.

Azarenkov, N. A., & Chibisov, D. (2019). High-frequency oscillations in plasma of lower hybrid cavities. *BAHT*, *122*, 24–26.

Balsley, B. B. (1964). Evidence of a stratified echoing region at 150 kilometers in the vicinity of the magnetic equator during daylight hours. *Journal of Geophysical Research*, *69*, 1925–1930.

Bell, T. F., & Ngo, H. D. (1988). Electrostatic waves stimulated by coherent VLF signals propagating in and near the inner radiation belt. *Journal of Geophysical Research*, *93*(A4), 2599–2618.

Berthelier, J. J., Malingre, M., Pfaff, R., Seran, E., Pottelette, R., Jasperse, J., et al. (2008). Lightning-induced plasma turbulence and ion heating in equatorial ionospheric depletions. *Nature Geoscience*, *1*, 101–105.

Bonnell, J. W., Schuck, P. W., Pinon, J.-L., Seyler, C. E., & Kintner, P. M. (1998). Observation of bound states and counter-rotating eigenmodes in the auroral ionosphere. *Physical Review Letters*, *80*(26), 5734–5737.

Booker, H. G., & Wells, H. W. (1938). Scattering of radio waves by the F region of the ionosphere. *Journal of Geophysical Research*, *35*(4), 249–256.

Buneman, O. (1963). Excitation of field aligned sound waves by electron streams. *Physical Review Letters*, *10*, 285–287.

Chang, T. (1993). Lower-hybrid collapse, caviton turbulence, and charged particle energization in the topside auroral ionosphere and magnetosphere. *Physics of Fluids B*, *5*(7), 2646–2656.

Chau, J. L., & Kudeki, E. (2006). Statistics of 150-km echoes over jicamarca based on low-power VHF observations. *Annales Geophysicae*, *24*(5), 1305–1310.

Chau, J. L., & Kudeki, E. (2013). Discovery of two distinct types of equatorial 150 km radar echoes. *Geophysical Research Letters*, *40*, 4509–4514.

Chibisov, D. V., & Mikhailenko, V. (2012). The lower hybrid waves driven by inhomogeneous ion-ring distribution. *Voprosy Atomnoj Nauki i Tekhniki*, *45*(33), 99–101.

Doolen, G. D., DuBois, D. F., & Rose, H. A. (1985). Nucleation of cavitons in strong langmuir turbulence. *Physical Review Letters*, *54*(8), 804–807.

Dovner, P. O., Eriksson, A. I., Boström, R., & Holback, B. (1994). Freja multiprobe observations of electrostatic solitary structures. *Geophysical Research Letters*, *21*(27), 1827–1834.

Dovner, P. O., Eriksson, A. I., Boström, R., & Holback, B. (1997). The occurrence of lower hybrid cavities in the upper ionosphere. *Neuroscience*, *24*(5), 619–622.

Eriksson, A. I., Holback, B., Dovner, P. O., & Bostrom, R. (1994). Freja multiprobe observations of electrostatic solitary structures. *Geophysical Research Letters*, *21*(27), 1827–1834.

Farley, D. T. (1963). A plasma instability resulting in field-aligned irregularities in the ionosphere. *Proceedings of the Royal Society of London. Series A, Mathematical and Physical Sciences*, *68*, 6083–6097.

Farley, D. T. (1969). Incoherent scatter correlation function measurements. *Radio Science*, *4*(10), 935–963.

Farley, D., Balsley, B. B., Woodman, R., & McClure, J. (1970). Equatorial spread F: implications of VHF radar observations. *Journal of Geophysical Research*, *75*, 7199.

Farley, D. T., Dougherty, J. P., & Barron, D. W. (1961). Scattering in a magnetic field. *Proceedings of the Royal Society of London. Series A, Mathematical and Physical Sciences*, *263*, 238–258.

Forbes, J. (1981). The equatorial electrojet. *Reviews of Geophysics*, *19*, 469.

Høymork, S., Pécseli, H. L., Lybekk, B., Trulsen, J., & Eriksson, A. (2000). The equatorial electrojet. *Journal of Geophysical Research*, *105*(A8), 18519–18535.

Huba, J. D. (1981). Diffusion of small-scale density irregularities during equatorial spread F. *Journal of Geophysical Research*, *7*(7), 9107–9114.

Huba, J. D., & Ossakow, S. L. (1979). On the generation of 3-m irregularities during equatorial spread F by low-frequency drift waves. *Journal of Geophysical Research*, *84*, 6697.

Huba, J. D., & Ossakow, S. L. (1981). Physical mechanism of the lower-hybrid-drift instability in a collisional plasma. *Journal of Atmospheric and Terrestrial Physics*, *43*(8), 775–778.

Hysell, D. L. (2000). An overview and synthesis of plasma irregularities in equatorial spread F. *Journal of Atmospheric and Solar-Terrestrial Physics*, *62*(12), 1037–1056.

Hysell, D. L., & Chau, J. L. (2006). Optimal aperture synthesis radar imaging. *Radio Science*, *41*, RS2003.

Hysell, D. L., Milla, M. A., & Woodman, R. F. (2017). Data-driven numerical simulations of equatorial spread F in the Peruvian sector. *Journal of Geophysical Research: Space Physics*, *122*(2), 2292–2299. https://doi.org/10.1002/2014JA019889

Hysell, D. L., Vierinen, J., & Sultzer, M. P. (2017). On the theory of the incoherent scatter gyrolines. *Radio Science*, *52*, 723–730.

Hysell, D. L., Vierinen, J., & Sultzer, M. P. (2019). The case for combining a large low-band very high frequency transmitter with multiple receiving arrays for geospace research: A geospace radar. *Radio Science*, *54*(7), 533–551.

Inan, U. S., & Bell, T. F. (1985). Spectral broadening of VLF transmitter signals observed on DEI: A quasi-electrostatic phenomenon? *Journal of Geophysical Research*, *90*, 1771.

Kintner, P. M., Vago, J., Chesney, S., Arnoldy, R. L., Lynch, K. A., Pollock, C. J., & Moore, T. E. (1992). Localized lower hybrid acceleration of ionospheric plasma. *Physical Review Letters*, *68*(16), 2448–2451.

Kjus, S. H., Pécseli, H. L., Lybekk, B., Holtet, J., Trulsen, J., Lür, H., & Eriksson, A. (1998). Statistics of the lower hybrid wave cavities detected by the freja satellite. *Journal of Geophysical Research*, *103*(A11), 26633–26647.

Knudsen, D. J., Wallis, D. D., & James, H. G. (1998). *ELF/VLF structures observed by OEDIPUS C*. Paper presented at the International Radio Science Meeting (pp. 5–8).

Kudeki, E., & Fawcett, C. D. (1993). High resolution observations of 150 km echoes at jicamarca. *Journal of Geophysical Research*, *20*(18), 1987–1990.

LaBelle, J., Kintner, P. M., Yau, A. W., & Whalen, B. A. (1986). Large amplitude wave packets observed in the ionosphere in association with transverse ion acceleration. *Journal of Geophysical Research*, *91*(A6), 7113–7118.

Lee, M. C., & Kuo, S. P. (1984). Production of lower hybrid waves and field-aligned plasma density striations by whistlers. *Journal of Geophysical Research*, *89*, 10873.

Lehmacher, G. A., Wu, H., Kudeki, E., Reyes, P., Hysell, D. L., & Milla, M. (2020). Height variation of gaps in 150-km echoes and whole atmosphere community climate model electron densities suggest link to upper hybrid resonance. *Journal of Geophysical Research*, *125*, e2019JA027204. https://doi.org/10.1029/2019JA027204

Longley, W. J., Oppenheim, M. M., Pedatella, N. M., & Dimant, Y. S. (2020). The photoelectron-driven upper hybrid instability as the cause of 150-km echoes. *Geophysical Research Letters*, *47*(8), 1–10. https://doi.org/10.1029/2020GL087391

Lynch, K. A., Arnoldy, R. L., Kintner, P. M., & Bonnell, J. (1996). The AMICIST auroral sounding rocketa comparison of transverse ion acceleration mechanisms. *Geophysical Research Letters*, *23*(8), 3293–3296.

Lynch, K. A., Arnoldy, R. L., Kintner, P., Schuck, P., Bonnell, J., & Coffey, V. (1999). Auroral ion acceleration from lower hybrid solitary structures: A summary of sounding rocket observations. *Journal of Geophysical Research*, *104*(A12), 28515–28534.

Malingre, M., Berthelier, J.-J., Pfaff, R., Jasperse, J., & Parrot, M. (2008). Lightning-induced lower-hybrid turbulence and trapped extremely low frequency (ELF) electromagnetic waves observed in deep equatorial plasma density depletions during intense magnetic storms. *Journal of Geophysical Research*, *113*(A11), 1–17.

McAdams, K. L., Labelle, J., Schuck, P. W., & Kintner, P. M. (1998). PHAZE ii observations of lower hybrid burst structures occurring on density gradients. *Geophysical Research Letters*, *25*(16), 3091–3094.

Morgan, M. G. (1979). Equatorial hiss in the topside ionosphere. *Journal of Geophysical Research*, *84*(A12), 7279–7287.

Musher, S. L., & Sturman, B. I. (1975). Collapse of plasma waves near the lower hybrid resonance. *Pis'ma v Zhurnal Eksperimental'noi i Teoreticheskoi Fiziki*, *22*(11), 537–542.

Musher, S. L., & Sturman, B. I. (1975). Collapse of plasma waves near the lower hybrid resonance. *JETP Letters*, *22*(11), 265–267.

Pécseli, H. L., Iranpour, K., Holter, O., Lybekk, B., Holtet, J., Trulsen, J., et al. (1996). Lower-hybrid wave cavities detected by the Freja-satellite. *Journal of Geophysical Research*, *101*(8), 5299.

Pécseli, H. L., Lybekk, B., Trulsen, J., & Eriksson, A. (1997). Lower-hybrid wave cavities detected by the Freja-satellite. *Plasma Physics and Controlled Fusion*, *39*(5A), 227–236.

Pinon, J., L., Kintner, P. M., Schuck, P., & Seyler, C. E. (1997). Observation and analysis of lower hybrid solitary structures as rotating eigenmodes. *Journal of Geophysical Research*, *102*(8), 17283–17296.

Rastogi, P. K., & Bowhill, S. A. (1976). Scattering of radio waves from the mesosphere-2. Evidence for intermittent mesospheric turbulence. *Journal of Atmospheric and Terrestrial Physics*, *38*(5), 449–468.

Robinson, P. A. (1996). Scalings, spectra, and statistics of strong wave turbulence. *Physics of Plasmas*, *3*(1), 192–201.

Robinson, P. A. (1999). Nonlinear lower hybrid solitary structures in auroral plasmas: comparison of theory with observations. *Advances in Space Research*, *23*(10), 1679–1688.

Rogister, A., & D'Angelo, N. (1970). Type2 irregularities in the equatorial electrojet. *Journal of Geophysical Research*, *75*(19), 3879–3887.

Schuck, P., Bonnell, J., & Kintner, P. (2003). A review of lower hybrid solitary structures. *IEEE Transactions on Plasma Science*, *31*, 1125–1176.

Schuck, P. W., Ganguli, G. I., & Kintner, P. M. (2002). On the role of lower hybrid collapse in the auroral ionosphere. *Physical Review Letters*, *89*(6), 065002.

Schuck, P., Seyler, C. E., Pinon, J.-L., Bonnell, J. W., & Kintner, P. M. (1998). Theory simulation and observation of bound states associated with lower hybrid solitary structures. *Journal of Geophysical Research*, *103*(A4), 6935–6953.

Seyler, C. (1994). Lower hybrid wave phenomena associated with density depletions. *Journal of Geophysical Research*, *99*(A10), 19513–19525.

Shapiro, V., Shevchenko, V. I., Solov'ev, G. I., Kalinin, V. P., Bingham, R., Sagdeev, R. Z., et al. (1993). Wave collapse at the lower hybrid resonance. *Physics of Fluids B*, *5*(9), 3148–3162.

Shukla, P. K., Bingham, R., & de Angelis, U. (1994). Large amplitude lower hybrid waves and associated nonlinear effects. *Physica Scripta*, *T50*, 75–80.

Sudan, R. N., Akinrimisi, J., & Farley, D. T. (1973). Generation of small-scale irregularities in the equatorial electrojet. *Journal of Geophysical Research*, *78*, 240–248.

Swanson, D. G. (2003). *Plasma waves, 2nd edition*. Auburn,AL: IOP Publishing Ltd.

Titova, E. E., Di, V. I., Yurov, V. E., Raspopov, O. M., Trakhtengertz, V. Y., Jiricek, F., et al. (1984). Interaction between VLF waves and turbulent ionosphere. *Geophysical Research Letters*, *11*(4), 323–326.

Treumann, R. A., & Baumjohann, W. (1997). *Advanced space plasma physics*. London, UK: Imperial College Press.

Vago, J. L., Kintner, P. M., Chesney, S., Arnoldy, R. L., Lynch, K. A., Moore, T., & Pollock, C. J. (1992). Transverse ion acceleration by localized lower hybrid waves in the topside auroral ionosphere. *Journal of Geophysical Research*, *97*(A11), 16935–16957.

Vakim, E., Mikhailenko, V. S., Stepanov, K. N., & Chibisov, D. (1997). Electrostatic instabilities of a multicomponent plasma with ions gyrating around the axis of the plasma column. *Physics Reports*, *23*(1), 44–52.

Varney, R. H., Swartz, W. E., Hysell, D. L., & Huba, J. D. (2012). SAMI2-PE: A model of the ionosphere including multistream interhemispheric photoelectron transport. *Journal of Geophysical Research*, *117*(A6), 4–16. https://doi.org/10.1029/2011JA017280

Woodman, R. F. (2009). Spread F-an old equatorial aeronomy problem finally resolved?. *Annals of Geophysics*, *27*(5), 1915–1934.